The Astrophysical Journal, 642:711–719, 2006 May 10

BLACK HOLE MASSES OF ACTIVE GALAXIES WITH DOUBLE-PEAKED BALMER EMISSION LINES[1]

Karen T. Lewis[2] and Michael Eracleous
Department of Astronomy and Astrophysics, Pennsylvania State University, 525 Davey Laboratory, University Park, PA 16802
Received 2005 June 13; accepted 2006 January 17

ABSTRACT

We have obtained near-IR spectra of five AGNs that exhibit double-peaked Balmer emission lines (NGC 1097, Pictor A, PKS 0921−213, 1E 0450.30−1817, and IRAS 0236.6−3101). The stellar velocity dispersions of the host galaxies were measured from the Ca II $\lambda\lambda$8494, 8542, 8662 absorption lines and were found to range from 140 to 200 km s^{-1}. Using the well-known correlation between the black hole mass and the stellar velocity dispersion, the black hole masses in these galaxies were estimated to range from 4×10^7 to 1.2×10^8 $M_\odot$. We supplement the observations presented here with estimates of the black holes masses for five additional double-peaked emitters (Arp 102B, 3C 390.3, NGC 4579, NGC 4203, and M81) obtained by other authors using similar methods. Using these black hole masses, we infer the ratio of the bolometric luminosity to the Eddington luminosity, ($L_{\rm bol}/L_{\rm Edd}$). We find that two objects (Pictor A and PKS 0921−213) have $L_{\rm bol}/L_{\rm Edd} \sim 0.2$, whereas the other objects have $L_{\rm bol}/L_{\rm Edd} \lesssim 10^{-2}$ (nearby, low-luminosity double-peaked emitters are the most extreme, with $L_{\rm bol}/L_{\rm Edd} \lesssim 10^{-4}$). The physical timescales in the outer regions of the accretion disks (at $r \sim 10^3 GM/c^2$) in these objects were also estimated and range from a few months for the dynamical timescale to several decades for the sound crossing timescale. The profile variability in these objects is typically an order of magnitude longer than the dynamical time, but we note that variability occurring on the dynamical timescale has not been ruled out by the observations.

Subject headings: accretion, accretion disks — black hole physics — galaxies: active — galaxies: nuclei

1. INTRODUCTION

During the past two decades, the number of active galactic nuclei (AGNs) known to exhibit broad, double-peaked Balmer emission lines has been steadily increasing. These lines were first observed in the broad-line radio galaxies (BLRGs) Arp 102B (Stauffer et al. 1983; Chen & Halpern 1989; Chen et al.1989), 3C 390.3 (Oke 1987; Perez et al. 1988), and 3C 332 (Halpern 1990) and are reminiscent of the double-peaked emission lines observed in cataclysmic variables, where they are regarded as the kinematic signature of the accretion disk (e.g., Horne & Marsh 1986). Thus, it was suggested by the above authors that the double-peaked emission lines originate in the accretion disk that fuels the AGN. A systematic survey of $z < 0.4$ BLRGs and radio-loud quasars was undertaken later on, and it was found that ~20% of the observed objects exhibited double-peaked Balmer lines (Eracleous & Halpern 1994, 2003). More recently, Strateva et al. (2003) found that 3% of the $z < 0.332$ AGNs in the Sloan Digital Sky Survey (SDSS; York et al. 2000) are double-peaked emitters.[3] Double-peaked emission lines have also been observed in low-ionization nuclear emission-line regions (LINERs; Heckman 1980) including NGC 1097 (Storchi-Bergmann et al. 1993), M81 (Bower et al. 1996), NGC 4203 (Shields et al. 2000), NGC 4450 (Ho et al. 2000), and NGC 4579 (Barth et al. 2001). Given the difficulty of detecting broad emission lines in LINERs (Ho et al. 1997), it is likely that a larger number of LINERs exhibit double-peaked emission lines. Although the known double-peaked emitters represent a small fraction of the total AGN population, they are an important and intriguing class of objects that deserve further study.

As described in detail by Eracleous & Halpern (2003), observational tests and basic physical considerations strongly suggest that the double-peaked Balmer lines originate in the outer regions of the accretion disk at distances from the black hole of hundreds to thousands of gravitational radii ($r_g = GM_{\rm BH}/c^2$, where $M_{\rm BH}$ is the mass of the black hole). The profiles of the double-peaked emission lines are observed to vary on timescales of years to decades and show occasional reversals in the relative strength of the red and blue peaks (for examples see Veilleux & Zheng 1991; Zheng et al. 1991; Gilbert et al. 1999; Shapovalova et al. 2001; Sergeev et al. 2000, 2002; Storchi-Bergmann et al. 2003; Gezari et al. 2004; Lewis et al. 2004a, 2004b; Lewis 2005; Gezari 2005). Intensive monitoring of 3C 390.3 shows that the time lag between variations in the continuum and the optical broad line is ~20 days (Dietrich et al. 1998; Sergeev et al. 2002); thus, the profile variations occur on much longer timescales than the light crossing time and seem to be unrelated to fluctuations in the ionizing continuum flux that take place on timescales of a few days to a few weeks. A similar effect is also observed in systematically monitored Seyfert galaxies (e.g., Wanders & Peterson 1996; Kassebaum et al. 1997). The profile variability is likely to be a manifestation of *physical* changes in the outer disk and the profile variability is thus a powerful tool that can be used to test models for dynamical behavior in accretion disks. Therefore, in the early 1990s a campaign was undertaken to systematically monitor a set of ~20 double-peaked emitters, including BLRGs from the Eracleous & Halpern (1994) sample and several LINERs.

Eracleous & Halpern (2003) and Strateva et al. (2003) found that the profiles of approximately 60% and 40%, respectively, of the double-peaked emitters from their samples can be fitted by a simple, axisymmetric accretion disk model. However, the long-term profile variability and the fact that in some objects the red peak is stronger than the blue peak (in contrast to the expectations of relativistic Doppler boosting) require the use of more

[1] Based on observations carried out at Cerro Tololo Inter-American Observatory, which is operated by AURA, Inc., under a cooperative agreement with the National Science Foundation.

[2] Current address: NASA Goddard Space Flight Center, Code 662, Greenbelt, MD 20771; ktlewis@milkyway.gsfc.nasa.gov.

[3] Strateva et al. (2003) find that double-peaked emitters are preferentially radio-loud; thus, the larger sample fraction among BLRGs is expected. See Strateva et al. (2003) for a description of the differences between these two samples.

general, nonaxisymmetric models. Some of the models that have been successfully employed to fit observed profiles include circular disks with orbiting bright spots (Arp 102B and 3C 390.3; Newman et al. 1997; Sergeev et al. 2000; Zheng et al. 1991) or spiral emissivity perturbations (3C 390.3, 3C 332, and NGC 1097; Gilbert et al. 1999; Storchi-Bergmann et al. 2003) and precessing elliptical disks (NGC 1097; Eracleous et al. 1995; Storchi-Bergmann et al. 1995, 1997, 2003).

To successfully interpret and model the long-term profile variability, it is not sufficient to reproduce the observed sequence of profiles; the variability must occur on a physical timescale that is consistent with the chosen model. The timescales of interest are the light crossing, dynamical, thermal, and sound crossing times, which are set by the black hole mass ($M_{\rm BH}$) and are given by Frank et al. (2002):

$$\tau_l = 6M_8\xi_3 \text{ days}, \quad (1)$$

$$\tau_{\rm dyn} = 30\tau_l\xi_3^{1/2} = 6M_8\xi_3^{3/2} \text{ months}, \quad (2)$$

$$\tau_{\rm th} = \tau_{\rm dyn}/\alpha = 5M_8\xi_3^{3/2} \text{ yr}, \quad (3)$$

$$\tau_s = 70M_8\xi_3T_5^{-1/2} \text{ yr}, \quad (4)$$

where $M_8 = M_{\rm BH}/10^8\ M_\odot$, $\xi_3 = r/10^3 r_g$, $T_5 = T/10^5$ K, and α ($\sim$0.1) is the Shakura-Sunyaev viscosity parameter (Shakura & Sunyaev 1973). The above models all predict variability on different timescales. For example, matter embedded in the disk orbits over $\tau_{\rm dyn}$, thermal instabilities will dissipate over $\tau_{\rm th}$, density perturbations, such as a spiral wave, precess on timescales that are an order of magnitude longer than $\tau_{\rm dyn}$ up to τ_s, and an elliptical disk will precess over even longer timescales.

Many of the models described above yield strikingly similar sequences of profiles. In order to determine which physical mechanism is responsible for the profile variability, it is necessary to connect the observed variability timescale (in yr) with one of the above *physical* timescales. Using an estimate of the black hole mass in NGC 1097, Storchi-Bergmann et al. (2003) estimated the physical timescales in the outer accretion disk that favored a spiral arm model over an elliptical disk model for this object. However, in order to discriminate between the above timescales, the black hole mass must be known to better than an order of magnitude and preferably to better than a factor of 3.

Another motivation for accurately estimating the black hole masses in the double-peaked emitters is to determine the accretion rate, relative to the Eddington accretion rate ($\dot{m}/\dot{m}_{\rm Edd}$), which is a diagnostic of the structure of the inner accretion flow. Because the local energy dissipation in the accretion disk is not always sufficient to power the observed Hα luminosity, Chen & Halpern (1989) proposed that the inner accretion flow in double-peaked emitters has the form of an ion torus (Rees et al. 1982) or a similar vertically extended, radiatively inefficient flow. This vertically extended structure would be able to illuminate the outer accretion disk and power the observed emission lines. For the well-studied Eracleous & Halpern (1994) sample there is considerable indirect observational support of this hypothesis, discussed fully in Eracleous & Halpern (2003), which is underscored by the growing number of LINERs known to sport double-peaked emission lines. The assumption that the inner accretion flow is radiatively inefficient is fundamental to the current ideas for the formation of the double-peaked emission lines and also the relationship between double-peaked emitters and the AGN population in general. Thus, it is extremely important to test this hypothesis more directly by obtaining estimates of the black hole masses, and thus $\dot{m}/\dot{m}_{\rm Edd}$, for double-peaked emitters.

Most of the double-peaked emitters are too distant to obtain black hole masses directly via spatially resolved stellar and gas kinematics. However, it is possible to determine the black hole masses indirectly through the well-known correlation between $M_{\rm BH}$ and the stellar velocity dispersion (σ) measured on the scale of the effective radius of the bulge (Ferrarese & Merritt 2000; Gebhardt et al. 2000; Tremaine et al. 2002). Therefore, we have begun a program to measure the stellar velocity dispersions in double-peaked emitters using the Ca II $\lambda\lambda$8594, 8542, 8662 triplet and present here the results for five objects. After obtaining estimates of the black hole masses via the $M_{\rm BH}$-σ relationship, the physical timescales in the outer accretion disk and $\dot{m}/\dot{m}_{\rm Edd}$ can be inferred for each object.

Here we focus specifically on measurements of the velocity dispersion in these double-peaked emitters to enable determinations of black hole masses. Although the timescales derived here are extremely valuable in modeling the long-term profile variability in these objects, a detailed discussion of the profile modeling is deferred to forthcoming papers. Preliminary results on modeling the profile variability (with the help of the black hole masses obtained here) can be found in Lewis (2005) and Gezari (2005).

This paper is organized as follows. In § 2 we describe the target selection, observations, and data reductions. The analysis of the data, including an examination of the various sources of error, is described in § 3, and the results and their implications are presented and discussed in § 4. In the Appendix we present a detailed description of the procedure used to correct the telluric water vapor absorption lines in these spectra. Throughout the paper we assume a *WMAP* cosmology ($H_0 = 70$ km s^{-1} Mpc^{-1}, $\Omega_M = 0.27$, $\Omega_\Lambda = 0.73$; Spergel et al. 2003).

2. SAMPLE SELECTION, OBSERVATIONS, AND DATA REDUCTION

Our primary motivation for obtaining robust black hole masses is to assist with modeling and interpreting the long-term profile variability of the double-peaked emitters. Therefore, we selected the targets that were part of the long-term monitoring campaign and have shown interesting variability. Absorption due to telluric water vapor becomes severe at wavelengths longer than 9200 Å, so only objects with $z < 0.062$ were selected. Finally, we only selected objects with declinations less than -5°. Five objects, NGC 1097, Pictor A, PKS 0921−213, 1E 0450.3−1817, and IRAS 0236.6−3101, met these criteria, and the properties of these objects are given in Table 1. All of our targets are hosted by elliptical galaxies or early-type spiral galaxies, whose stellar spectra in the Ca II region are dominated by G and K giants (Worthey 1994). Therefore, we observed numerous G and K giant stars, with spectral types ranging from K5 to G6, to serve as stellar templates. The stars used in the final fits are listed in Table 2.

The spectra were obtained on 2003 December 4–8 using the Ritchey-Chrétien (RC) spectrograph on the 4 m Blanco telescope at the Cerro Tololo Inter-American Observatory. The G380 grating was used in conjunction with the RG 610 order-separating filter, and the spectra covered the range from 7690 to 9350 Å. The slit had a width of 1.″33 and was oriented east to west. The resulting spectral resolution was 1.35 Å FWHM, as measured from the arc lamp spectra, corresponding to a velocity resolution of $\sim$50 km s^{-1}. The galaxies and the template stars were observed at an air mass of less than 1.13, and differential atmospheric refraction was not significant over the small wavelength interval of interest. The atmospheric seeing during the observations of the galaxies was less than 1.″5 and frequently

TABLE 1
Galaxy Properties

Galaxy Name	z[a]	f_ν(8500 Å)[b] (mJy)	Extraction Size (arcsec, kpc)	Exposure Time (s)	S/N[c]
NGC 1097	0.0043	26.0	5.0, 0.45	5400	115
Pictor A	0.035	3.0	4.5, 3.3	18000	45
PKS 0921−213	0.0531	3.0	7.0, 7.7	14400	40
1E 0450.3−1817	0.0616	0.5	5.0, 6.1	18000	25
IRAS 0236.6−3101	0.0623	3.2	5.5, 7.1	12600	80

[a] Redshifts taken from Eracleous & Halpern (2004).
[b] These fluxes were determined from spectra taken with a narrow slit and can thus be uncertain by up to a factor of 2.
[c] S/N per pixel in the continuum regions in the vicinity of the Ca II triplet absorption lines.

less than 1.″0, although some of the template stars were observed with seeing as large as 2.″0.

A set of bias frames and HeNeAr comparison lamp spectra were taken at the beginning and end of each night, and quartz flats were taken immediately preceding or following each galaxy exposure. Rapidly rotating B stars (with rotational velocities in excess of 200 km s^{-1}) were observed periodically throughout the night at similar air mass as the galaxies and template stars and were used to correct for the deep telluric water vapor lines at wavelengths longer than 8900 Å (in the galaxies) and shorter than 8400 Å (in the template stars). The exposure times for the galaxies are listed in Table 1.

The primary data reductions (the bias level correction, flat-fielding, sky subtraction, removal of bad columns and cosmic rays, extraction of the spectra, and wavelength calibration) were performed using the Image Reduction and Analysis Facility (IRAF).[4] The night-sky emission was estimated by fitting a third-order spline along the spatial direction to two intervals (with widths of 10–20 pixels) located on either side of the spectral extraction region. In most objects, with the exception of Pictor A, the Ca II region was not heavily contaminated by night-sky emission lines. The issue of sky subtraction is discussed further in § 3.1. The difference in dispersion solutions from one night to the next was less than 0.1%, so the same dispersion solution was applied to the spectra from all five nights. It was not possible to obtain comparison lamp spectra before or after each galaxy spectrum was taken. However, measurements of the night-sky lines, which are largely unblended at this resolution, were used to fine-tune the wavelength solution for the galaxy spectra before they were combined; this ensured that the combined spectra were not artificially broadened. The applied shifts were generally less than 1 Å. The error spectrum was calculated by adding in quadrature the Poisson noise in the spectra of the night sky and the object spectrum (prior to the removal of cosmic rays and bad columns).

[4] IRAF is distributed by the National Optical Astronomy Observatory, which is operated by the Association of Universities for Research in Astronomy, Inc., under cooperative agreement with the National Science Foundation.

TABLE 2
Template Stars

Star Name	Spectral Type	Star Name	Spectral Type
HD 3013	K5 III	HD 21	K1 III
HD 79413	K1 III	HD 3809	K0 III
HD 3909	K4 III	HD 2224	G8 III
HD 2066	K3 III	HD 5722	G7 III
HD 225283	K2 III	HD 14834	G6 III

None of the host galaxies in our sample have a reported value of the effective radius, and in all cases except NGC 1097 and Pictor A, suitable images were not available from which to determine the effective radius. To obtain a rough estimate of the effective radius, the spectra were collapsed along the spectral direction to obtain a spatial profile, which was then fitted with the sum of a de Vaucouleurs ($R^{1/4}$) profile and an AGN point source convolved with a Gaussian, and background. The effective radius determined for Pictor A from a ground-based image was in agreement with that obtained from the spatial profile. There was considerable uncertainty in the effective radii, however, and we chose to extract the spectra using the smallest effective radius allowed by the data (see also the discussion in § 3.2). In the case of NGC 1097, which is a spiral galaxy with a nuclear star-forming ring, the extraction radius was chosen to lie just within the star-forming ring (see § 3.3 for more details). The extraction radii used for the galaxies are listed in Table 1.

The removal of the telluric water vapor lines at wavelengths longer than 8900 Å was an essential step in the data reductions because many of the Ca II lines in the observed galaxies were redshifted into this region of the spectrum. As described in detail in the Appendix, a telluric template of the atmospheric transmission was derived from the spectrum of a rapidly rotating B star. The spectra obtained from individual exposures of the galaxies were divided by this telluric template, allowing for the possibility of a slight wavelength shift between the template and galaxy spectra. Because the humidity was quite low and stable throughout the run (25%–35%) and all of our objects were observed at low air mass, we found that it was possible to correct all of the galaxies with the same telluric template.

The spectra of the G and K giant stars, as well as those from individual exposures of the galaxies, were normalized with a low-order polynomial. In most instances, the averaged galaxy spectra could be successfully fitted without any further normalization. However, the spectrum of NGC 1097 was renormalized with a low-order polynomial in the region of the Ca II triplet. The resulting galaxy spectra and a representative template star are shown in Figure 1. The average signal-to-noise ratios (S/Ns) of the galaxy spectra are listed in Table 1; the S/N of the stellar templates ranged from 150 to 300.

3. ANALYSIS AND RESULTS

3.1. *Fitting Method*

The velocity dispersions in the host galaxies of these five AGNs were determined by directly fitting the galaxy spectra with a model given by

$$M(\lambda) = fT(\lambda) \otimes G(\lambda) + P(\lambda), \quad (5)$$

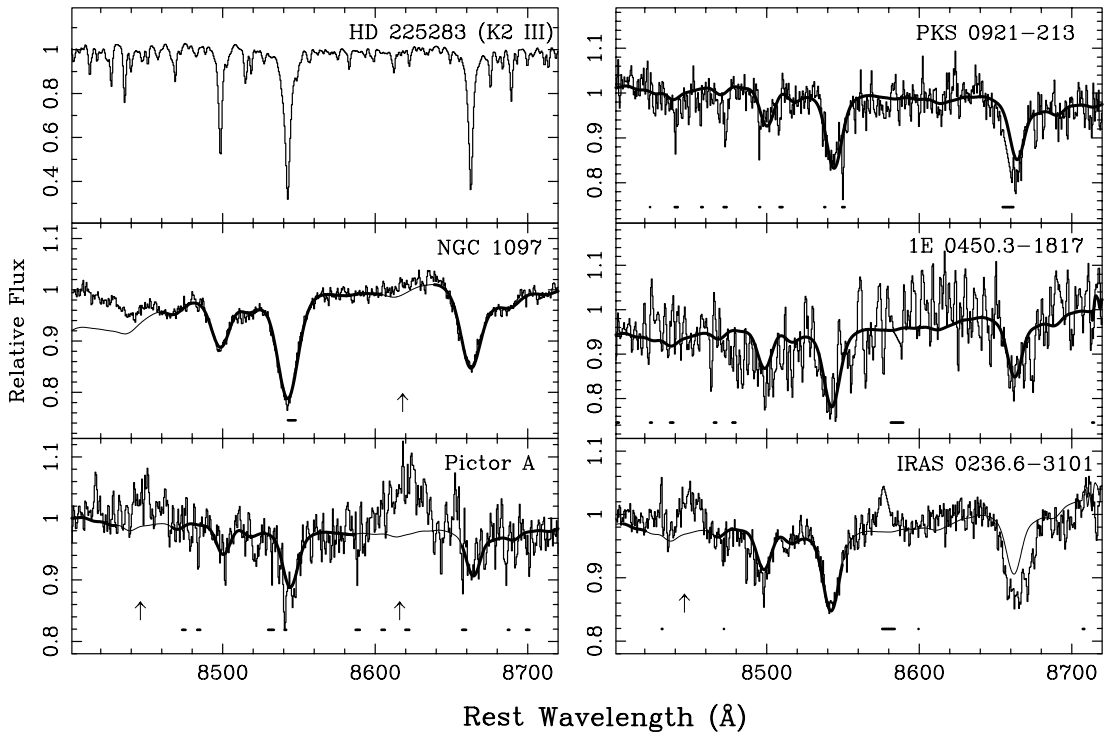

FIG. 1.—Ca II spectral region in a template star and the five target galaxies. The best-fitting model for each galaxy is overplotted, and in the intervals used to perform the fit, the model is overplotted with a thick solid line. Data points with unusually large error bars, due to a strong night-sky line, a cosmic ray, or a bad column, are indicated with black dots along the bottom of the spectrum. The O I λ8446 and [Fe II] λ8618 emission lines, when present, are indicated by an arrow.

where $T(\lambda)$ is a stellar template, $f(<1)$ is a dilution factor, $G(\lambda)$ is a Gaussian with a dispersion σ, $P(\lambda)$ is a low-order (first or second order) polynomial, and $\otimes$ denotes a convolution. The stellar template was either an individual G or K giant star or a linear combination of G and K giants (with weights of 25% and 75%, respectively, following Worthey 1994). The fitting intervals were selected to exclude emission lines (O I λ8446 and [Fe II] λ8618); however, it was not necessary to explicitly exclude pixels contaminated by strong night-sky emission lines, bad columns, or cosmic rays. The large error bars on such data points resulted in these data being effectively ignored in determining the best-fitting model.

To find the best-fitting velocity dispersion and its uncertainty, we scanned the two-dimensional parameter space defined by σ and f in small steps. The coefficients of the low-order polynomial describing the nonstellar continuum were evaluated at each grid point by minimizing the χ^2 statistic. For all of the galaxies, including NGC 1097, the value of χ^2 per degree of freedom (χ^2_ν) for the best fit was typically $\chi^2_\nu \sim 3$. This large value of χ^2_ν suggests that the error bars on the flux density of the pixels in the spectra were underestimated, and in fact the rms dispersion of the data in featureless regions of the spectra was typically 1.5–1.9 times larger than the formal error bars assigned to the individual pixels. We attribute this increased scatter to imperfect subtraction of the strong night-sky emission lines appearing throughout our spectral range (this was caused by curvature of the sky lines along the direction of the slit). We note that the discrepancy between the rms deviation and the formal error bars is only slightly greater at wavelengths larger than 8900 Å, where the telluric absorption correction was performed. If we increased the error bars on the spectral pixels by the above factor, the best-fit models would have had $\chi^2_\nu \sim 1$ in most cases. Thus, the values of χ^2 for each fit were rescaled such that $\chi^2_\nu \equiv 1$ and the 68% confidence error contour in σ and f was defined by $\Delta\chi^2 = 2.3$. This is equivalent to the practice of rescaling the error bars on each pixel, adopted by Barth et al. (2002). The galaxy spectra and their best-fitting models are shown in Figure 1.

The use of a direct fitting method for determining velocity dispersions has been well tested by Barth et al. (2002), and Garcia-Rissmann et al. (2005) demonstrate that the results obtained with direct fitting are consistent with those obtained through the Fourier correlation quotient method (see, e.g., Bender 1990). Nevertheless, we also conducted our own tests using simulated spectra that were generated from a broadened K2 III stellar template (plus a featureless continuum) to which random noise was added. In our simulated spectra, the velocity dispersion ranged from 100 to 200 km s^{-1}, the dilution factor (f) varied from 0.6 to 1.0, the order of the featureless continuum ranged from 0 to 2, and the S/N of the spectra ranged from 35 to 100. After generating 10 realizations of each simulated spectrum, we found that our direct fitting method successfully recovered the input velocity dispersion within the 68% error interval determined from the fit. This was the case even when the order of the polynomial representing the featureless continuum was forced to be different from that used to generate the spectra. Of course, the error bar on the best-fit stellar velocity dispersion was larger for spectra with lower S/N and/or larger velocity dispersion and dilution factor. We also tested our implementation of the direct fitting method, which differs slightly from that used by Barth et al. (2002), by using our code to fit the data for Arp 102B obtained by these authors. Within the error bars, we obtain the same velocity dispersion as these authors.

3.2. *Sources of Systematic Error*

There are some potential sources of systematic error that were not accounted for by the error analysis described above:

1. *Extraction size.*—The effective radii of the galaxies determined here are quite uncertain; however, we found that best-fit

velocity dispersion was not sensitive to the extraction radius. We also note that the S/N of the spectra was not significantly affected by the extraction radius, with the exception of Pictor A, which is discussed further in § 3.3.

2. *Telluric absorption correction*.—Although considerable care was taken to perform the telluric absorption correction, the telluric template is most likely overestimated in the interval from 9195 to 9215 Å, as described in detail in the Appendix. Consequently, the telluric correction in this interval is not complete and the flux in the corrected galaxy spectra could be underestimated by as much as 4%. This artifact cannot be accounted for in any statistical way; however, when it is obvious in the spectra, this interval is not included in the fit.

3. *Template mismatch*.—An important advantage of using the Ca II triplet to measure the stellar velocity dispersion is the fact that the strength of the absorption lines is relatively insensitive to the stellar population (Pritchet 1978; Dressler 1984). We found that the rms scatter in the values of σ obtained using the different templates (both individual stars and linear combinations of stars) was only a few kilometers per second. This is consistent with the rms spread we obtain when fitting high-S/N simulated spectra with stellar templates that were different than that used to generate the spectrum. This template mismatch represents an additional error that is not accounted for by our fitting procedure, which only explores a range in σ and f. We treat this rms spread as an additional error that we add in quadrature to the 68% error bar for NGC 1097, similarly to Barth et al. (2002). For the other galaxies the uncertainty due to template mismatch was negligible compared to the uncertainty on the best fit and was not included.

3.3. *Notes on Individual Objects*

NGC 1097.—The nuclear structure of the barred spiral galaxy NGC 1097 is extremely complicated, as evidenced by ^{12}CO observations that suggest the presence of a cold nuclear disk being fed by matter streaming along the bar (Emsellem et al. 2001). These authors find that within the inner 5″, the velocity dispersion ranges from 145 km s^{-1} in the center to 220 km s^{-1} at the inner edge of the bar, as measured from the broadening of the CO band head. There is a star-forming ring extending from 5″ to 10″, as mapped by Hα and radio emission (Hummel et al. 1987), which is mostly excluded in our data. However, Storchi-Bergmann et al. (2005) recently demonstrated that there is a starburst within 0.″1 (9 pc) of the central black hole. Despite these difficulties, we obtained an excellent fit to the data using a single K giant star, although the featureless continuum is more complex and must be described with a third-order polynomial. The interval 8600–8640 Å (rest wavelength) was excluded from the fit because contamination from [Fe II] emission might be responsible for the poor fit to the data in this interval. If this interval is included in the fit, the best-fit velocity dispersion increases to 208 ± 5 km s^{-1}.

Pictor A.—The Ca II triplet is located in the region of the spectrum with the strongest night-sky emission lines. Although the effective radius was estimated to be 9″ (6.5 kpc), the use of a smaller extraction radius (4.″5) allowed for a much improved subtraction of the night-sky emission and consequently an increased S/N and a decrease in the error bars. When a 9″ extraction radius was used, the best-fit velocity dispersion was the same, although the error bars were larger. Both O I and [Fe II] emission lines are present in the spectrum, and the regions around these lines were ignored in the fit.

PKS 0921−213.—The Ca II λ8662 line is strongly contaminated by several bad columns, and as a result, the blue side of this line does not contribute to the determination of the velocity dispersion.

1E 0450.3−1817.—This object is extremely faint and the S/N is much lower than for the other objects (S/N $\sim$ 15 pixel^{-1}). Therefore, the spectrum was smoothed by a 3 pixel wide boxcar function in order to increase the S/N ($\sim$25 pixel^{-1}). The best-fit velocity dispersion is the same as when the unsmoothed spectrum is fitted, but the error bars are decreased by $\sim$30%. We have verified that for NGC 1097 and IRAS 0236.6−3101 neither the best-fit velocity dispersion nor the uncertainty is changed when the spectra are similarly smoothed.

IRAS 0236.6−3101.—The Ca II λ8662 line has an observed wavelength of 9202 Å, which places this line in the region of the telluric template that was underestimated, as described in § 3.2 and the Appendix. The λ8662 line is deeper than would be expected based on the strength of the two other Ca II lines, and we chose to ignore this line when performing the fit. If this line were included, the best-fit value of σ would increase to $\sim$200 km s^{-1}; however, a model with this large velocity dispersion is an extremely poor fit to the λ8542 line. An O I emission line is present, and the interval around this line was excluded from the fit.

4. DISCUSSION AND CONCLUSIONS

Using the measurements of the velocity dispersion found above, we determine the black hole masses, the Eddington ratios, and the physical timescales in the accretion disk. All of these quantities are given in Table 3. The black hole masses were estimated via the $M_{\rm BH}$-σ relationship (Tremaine et al. 2002), namely,

$$\log\left(\frac{M}{M_\odot}\right) = \alpha + \beta \log\left(\frac{\sigma}{\sigma_0}\right), \tag{6}$$

where $\alpha = 8.13 \pm 0.06$, $\beta = 4.02 \pm 0.32$, and $\sigma_0 = 200$ km s^{-1}. The scatter in the $M_{\rm BH}$-σ relationship is not included in the error, but the error bars on the coefficients are. For completeness, we include in this table the double-peaked emitters with stellar velocity dispersions reported in the literature, namely, Arp 102B, NGC 4203, NGC 4579 (Barth et al. 2002), and 3C 390.3 (Nelson et al. 2004). We also include M81, for which a mass estimate of $\sim 6 \times 10^7$ $M_\odot$ is based on resolved stellar and gas kinematics (Bower et al. 2000 and Devereux et al. 2003, respectively). The inferred black hole masses for these 10 objects range from 4×10^7 to 5×10^8 $M_\odot$.

We note that the estimate of the black hole mass for NGC 4203 used here ($M_{\rm BH} \sim 6 \times 10^7$ $M_\odot$) is in disagreement with the results of Shields et al. (2000) and Sarzi et al. (2001), who placed an upper limit of 6×10^6 $M_\odot$ on the black hole mass from spatially resolved gas kinematics. As noted by Shields et al. (2000), the gas need not lie in a flat disk and it could be subject to nongravitational forces; in the particular case of NGC 4203, the disk is suspected to be warped (Sarzi et al. 2001). Thus, we have chosen to use the mass obtained from the stellar velocity dispersion.

The physical timescales in the outer accretion disk were computed using equations (2)–(4), assuming that $\xi_3 = 1$, $\alpha = 0.1$, and $T_5 = 1$. For these black hole masses, the dynamical timescale ranges from a few months to 1 yr, the thermal timescale ranges from 1 yr to a decade, and the sound crossing timescale ranges from a decade to 100 yr. The observed profile variations occur on timescales of several years (see, e.g., Lewis 2005; Gezari 2005) for most objects, which is an order of magnitude longer than the dynamical timescales found here. This strongly suggests that in general the profile variability might be due predominantly to either a thermal phenomenon or the precession

TABLE 3
VELOCITY DISPERSIONS AND DERIVED PROPERTIES

Galaxy Name	σ (km s^{-1})	M_{BH} ($10^7\ M_\odot$)	$L_{2-10\,keV}$ (ergs s^{-1})	X-Ray References	L_X/L_{bol}	L_X/L_{bol} References	Range in L_{bol}/L_{Edd}	τ_{dyn} (months)	τ_{th} (yr)	τ_s (yr)
NGC 1097	196 ± 5	12 ± 2	4.4×10^{40}	1	0.09	10	$(2–3) \times 10^{-5}$	6–8	5–7	70–100
Pictor A	145 ± 20	4 ± 2	4.0×10^{43}	2, 3	0.07	11	0.08–0.3	1–4	1–3	15–40
PKS 0921−213	144^{+18}_{-16}	4 ± 2	4.2×10^{43}	4	0.07	11	0.09–0.3	1–4	1–3	15–40
1E 0450.3−1817	150^{+30}_{-25}	4^{+4}_{-3}	3.2×10^{42}	5	0.13	12	$(0.2–2) \times 10^{-2}$	0.5–5	0.5–4	10–55
IRAS 0236.6−3101	154 ± 15	5 ± 2	7.3×10^{42}	6	0.13	12	$(0.6–2) \times 10^{-2}$	2–4	2–3	35–50
Arp 102B	188 ± 8 [a]	11 ± 2	6.3×10^{42}	7	0.17	13	$(1–2) \times 10^{-3}$	5–8	4–7	60–90
3C 390.3	273 ± 16[b]	50 ± 10	1.9×10^{44}	3	0.11	14	$(2–4) \times 10^{-2}$	20–40	17–30	230–430
NGC 4579	165 ± 4 [a]	6 ± 1	2.0×10^{41}	8	0.20	15	$(1–2) \times 10^{-4}$	3–4.5	2.5–4	35–50
NGC 4203	167 ± 3 [a]	6 ± 1	4.0×10^{40}	9	0.13	12	$(3–4) \times 10^{-5}$	3–4.5	2.5–4	35–50
M81	...	6 ± 1[c]	1.9×10^{40}	8	0.09	15	$(2–3) \times 10^{-5}$	3–4	2.5–4	35–50

[a] Velocity dispersions taken from Barth et al. (2002).
[b] Velocity dispersion taken from Nelson et al. (2004).
[c] Black hole mass taken from Bower et al. (2000) and Devereux et al. (2003); derived from spatially resolved stellar and gas kinematics, respectively.

REFERENCES.—(1) Nemmen et al. 2004, 2006; (2) Eracleous & Halpern 1998; (3) Sambruna et al. 1999; (4) K. T. Lewis et al. 2006, in preparation; (5) Stocke et al. 1983; (6) Boller et al. 1992; (7) Eracleous et al. 2003; (8) Ho 1999; (9) Iyomoto et al. 1998; (10) Nemmen et al. 2004, 2006; (11) assumed radio-loud QSO SED of Elvis et al. 1994; (12) assumed average L_X/L_{bol} for the LINERs in this study; (13) SED from compilation in Eracleous et al. 2003 (without the IR bump) except the X-ray flux density was scaled to match the *ROSAT* 0.5–2.0 keV flux (Halpern 1997); (14) SED compiled from Alef et al. 1988 (radio), Miley et al. 1984 (IR), Veilleux & Zheng 1991 (optical), Zheng 1996 (UV), and Malaguti et al. 1994 (X-ray); (15) Ho 1999.

of a large-scale emissivity pattern (e.g., a spiral arm). One exception is Arp 102B, in which the relative fluxes of the red and blue peaks of the profile varied sinusoidally with a period of 2 yr (of the same order as the dynamical time) over an interval of 4 yr (Newman et al. 1997). A very similar variability pattern, with the same period, also appeared 5 yr later (Gezari 2005). We also note that in addition to gross profile variability that occurs on timescales of years, some objects also exhibit sporadic variability on timescales of only a few months; these variations may be related to a phenomenon that occurs on the dynamical timescale.

The light crossing time of the disk of 3C 390.3 computed from equation (1) is in the range of 11–37 days (using the inner and outer radii of the line-emitting disk from Eracleous & Halpern 1994). This affords an immediate test of the disk interpretation of the double-peaked lines. A reverberation mapping campaign by the International AGN Watch (Dietrich et al. 1998) yielded a lag between the continuum and Balmer line variations of approximately 20 days, which is in good agreement with the above value.

The Eddington ratios were computed by comparing the total bolometric luminosity to the Eddington luminosity [$L_{Edd} = 1.38 \times 10^{38}(M_{BH}/M_\odot)$ ergs s^{-1}]. We used the available spectral energy distributions (SEDs) and integrated bolometric luminosities for M81, NGC 4579 (Ho 1999), and NGC 1097 (Nemmen et al. 2004, 2006). Eracleous et al. (2003) presented an SED for Arp 102B, and we adopt their SED, excluding the IR bump and adjusting the specific luminosity in the X-ray band.[5] An SED for 3C 390.3 was compiled from various sources in the literature, and the full references are provided in Table 3. There are no SEDs for the remaining objects, and we estimated their bolometric luminosities using their measured X-ray luminosities and assuming a value for $L_{2-10\,keV}/L_{bol}$, as given in Table 3. For IRAS 0236.6−3101, 1E 0450.3−1817, and NGC 4203 we adopted the average $L_{2-10\,keV}/L_{bol}$ for the LINERs in this study (Arp 102B, NGC 1097, M81, and NGC 4579). For Pictor A and PKS 0921−213 we adopted the radio-loud quasar SED of Elvis et al. (1994) since this is the most likely SED for these objects (had we adopted the LINER-like SED, even the lower limit to the Eddington ratio would be larger than 10^{-2}). To compute L_{bol}, the SEDs were integrated from 1 MHz to 100 keV, using power-law interpolations between data points. We note that the 2–10 keV flux of an AGN is variable by a factor of a few, which implies an additional uncertainty to the bolometric luminosities estimated from the X-ray luminosity.

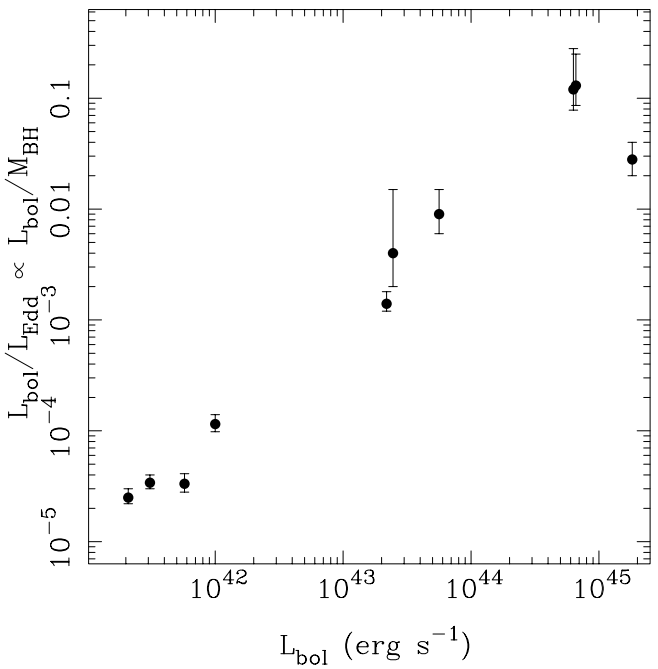

FIG. 2.—Plot of Eddington ratio vs. the bolometric luminosity. See Table 3 for the data and § 4 for details on how these quantities were obtained. The apparent trend is very likely artificial since the estimated black hole masses span only a factor of 10 (a factor of 2, if 3C 390.3 is excluded), while the bolometric luminosities span a factor of 10^4. Moreover, 3C 390.3 has L_{bol} that is 2 orders of magnitude larger than IRAS 0236.6−3101 and 1E 0450.4−1817, yet its Eddington ratio is similar.

[5] We adopted $\log[\nu L_\nu(1\ keV)] = 42.331$ for consistency with earlier observations with the *ROSAT* and *Einstein* X-ray observatories (Halpern 1997; Biermann et al. 1981). During the *ASCA* observation (Eracleous et al. 2003), the X-ray flux was found to be a factor of 3 higher than the earlier observations and was attributed to an unusually high state. We retained the 2–10 keV spectral slope measured from the *ASCA* X-ray spectrum.

The Eddington ratios listed in Table 3 span a wide range, and there is a general positive trend between bolometric luminosity and Eddington ratio, which we illustrate in Figure 2. However, we do not consider this trend convincing because the quantities plotted are not independent of each other ($L_{\rm bol}/L_{\rm Edd} \propto L_{\rm bol}/M_{\rm BH}$). The trend is merely a consequence of the fact that the estimated black hole masses span only a factor of 10 (a factor of 2, if 3C 390.3 is excluded), while the bolometric luminosities span a factor of 10^4. The existence of such a trend is also called into question by the fact that 3C 390.3 has $L_{\rm bol}$ that is 2 orders of magnitude larger than IRAS 0236.6−3101 and 1E 0450.4−1817, yet its Eddington ratio is similar.

While many double-peaked emitters may harbor radiatively inefficient accretion flows, the accretion flows in some objects, such as Pictor A and PKS 0921−213, are probably more similar to those found in Seyfert 1 galaxies. A vertically extended structure may still be required in these objects to illuminate the outer accretion disk and may take the form of a spherical corona such as that used by Dumont & Collin-Souffrin (1990), a beamed corona (Beloborodov 1999; Malzac et al. 2001), and/or the base of the jet (Markoff et al. 2001).

That the double-peaked emitters in even this small sample have a wide range of Eddington ratios is not completely surprising. The double-peaked emitters found in the SDSS by Strateva et al. (2003) are very heterogeneous. Although 12% were classified as LINERs, many others had properties that were indistinguishable from the general $z < 0.332$ AGN population. We note that our results confirm the general findings of Wu & Liu (2004), who estimated black hole masses for both the Eracleous & Halpern (1994) and Strateva et al. (2003) samples through a series of correlations obtained from reverberation mapping of AGNs (Kaspi et al. 2000). These authors found that (1) double-peaked emitters are a heterogeneous group with a wide range in Eddington ratios and (2) those objects with higher bolometric luminosities tend to have larger Eddington ratios. However, the black hole masses of individual double-peaked emitters deduced through that method can be very inaccurate, as acknowledged by these authors. Although the black hole masses for 1E 0450.3−1817 and Arp 102B inferred by these authors are consistent with those obtained through the $M_{\rm BH}$-σ relationship, the black hole masses for Pictor A and IRAS 0236.6−3101 were overestimated by an order of magnitude. Thus, we caution that for the purposes of modeling and interpreting individual objects, it is necessary to obtain black hole masses through a method that is more well tested and well calibrated in the range of BH masses relevant to our objects, such as the $M_{\rm BH}$-σ relationship.

K. T. L. was funded by the NASA Graduate Research Fellows Program (NGT5-50387). We thank the CTIO staff for their expert help during the observing run and the Association of Universities for Research in Astronomy for financial support for travel to the observatory. We are grateful to Aaron Barth, Steinn Sigurdsson, and the anonymous referee for helpful discussions and suggestions. We thank A. Barth for allowing us to use his spectra to test our fitting method.

APPENDIX

TELLURIC CORRECTION

Removal of the telluric water vapor absorption lines was an essential component of the data reductions because, with the exception of NGC 1097, at least one of the Ca II absorption lines in each target galaxy was embedded in the telluric water vapor lines at wavelengths longer than 8900 Å. To illustrate this, we show in Figure 3 the uncorrected spectrum of IRAS 0236.6−3101 in which all three Ca II lines are embedded in the telluric water vapor bands. To create a template of the atmospheric transmission, it is common to observe an object with a nearly featureless continuum in which any sharp features can be attributed to atmospheric absorption. The atmospheric transmission changes not only with position in the sky and air mass but also throughout the night. Because we wished to observe telluric standards several times each night, we opted to observe rapidly rotating B stars, with rotational velocities in excess of 200 km s^{-1}. Although these stars are not as featureless as white dwarfs, they have the advantage of being more common, allowing us to find a telluric standard in a similar region of the sky as our targets. More importantly, they are very bright, requiring only ∼30 s of exposure.

Despite the rotational broadening, the hydrogen Paschen lines were still narrow enough that they could not be fitted as part of the continuum as shown in Figure 4. We modeled the intrinsic spectrum of the B star as a combination of a low-order ($n < 4$) polynomial and a set of Paschen absorption lines represented with Voigt profiles. The best-fit Voigt profile parameters were determined by fitting the interval from 8650 to 8875 Å, a portion of the B star spectrum that had only three relatively unblended Paschen lines and was free from

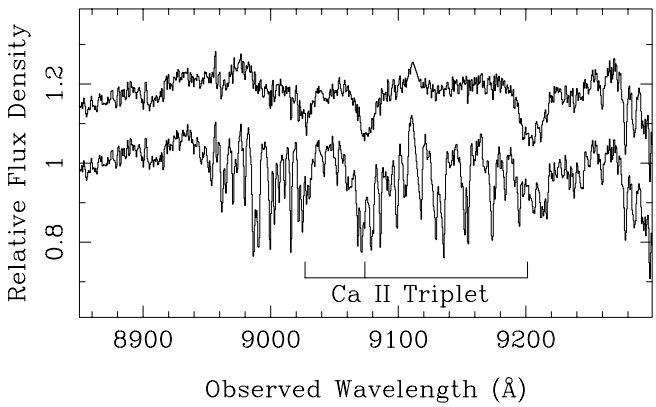

FIG. 3.—Average of the IRAS 0236.6−3101 spectra in the absence of telluric correction. The positions of the Ca II triplet lines are marked. For comparison, the final spectrum obtained when the telluric correction is performed is overplotted, with an arbitrary vertical offset.

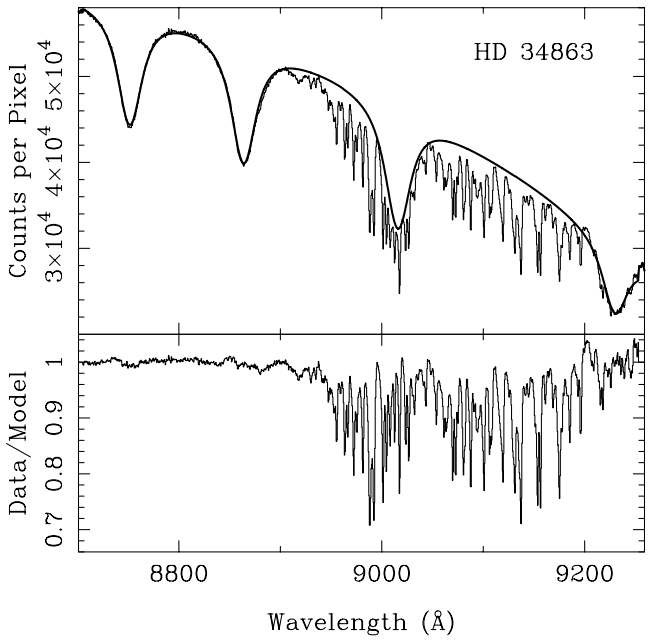

FIG. 4.—*Top*: Spectrum of the rapidly rotating star HD 23683 (*histogram*) and the best-fitting model for its continuum and hydrogen Paschen lines (*solid line*). *Bottom*: Residuals to the fit, which are used as a template of the telluric water vapor lines. Before this template is applied to the galaxy spectra, the values at $\lambda < 8900$ Å are set to unity and the rest of the template is renormalized with a first-order polynomial.

telluric absorption lines. Restricting the profile parameters (except for their strengths) to narrow ranges around the best-fit values, the B star spectrum was then fitted over the 8725–9300 Å interval, which included four Paschen lines, two of which were fitted in the previous step. A sequence of rejection iterations was performed, in which the lower rejection level became progressively more strict so as to force the fit to model the upper envelope of the spectrum. An example of this fit is shown in Figure 4. The B star spectrum was then divided by this model fit to generate a template of the telluric absorption lines, and this telluric template was set to unity at wavelengths less than 8900 Å.

The residual template still exceeded unity near the red end of the spectrum, particularly in the interval from 9195 to 9215 Å, located on the blue wing of the Paζ λ9229.75 line. The depth of this Paschen line was underestimated because there was not sufficient spectral coverage redward of the line to determine the true continuum level (see Fig. 4). A first-order polynomial was fitted post facto to the envelope of the template to ensure that all values were less than unity. Nevertheless, we suspect that the telluric template is overestimated by as much as 4% in the interval 9195–9215 Å, and we exercise caution when using the template over this range of wavelengths. The only object affected by this defect is IRAS 0236.6−3101, where the Ca II λ8662 line appears to be too deep; the impact of this is discussed in § 3.3. If one plans to use telluric templates derived from rapidly rotating B stars near 9200 Å, it is advisable to have sufficient spectral coverage redward of the Paζ line so that the continuum level (and thus the true line depth) can be determined.

Of the six rapidly rotating B stars observed, the simple Voigt profile model described above only yielded a satisfactory fit (i.e., residuals less than 1%) in HD 34863. However, the humidity was fortunately low and extremely stable over the course of the observing run. When the template derived from HD 34863 was applied to the other rapidly rotating B stars, the residuals were less than 3% in all cases and sometimes less than 1%; thus, we were able to apply this single template to all of the galaxy spectra with little additional degradation in the S/N.

The telluric absorption lines are not resolved in these data, and it is possible that the lines are so severely blended that they form a pseudocontinuum that would not be corrected for by our method. However, we have verified that this is not the case. A spectrum of the telluric water vapor lines derived from a high-resolution ($\Delta\lambda/\lambda \sim 150{,}000$) near-IR spectrum of Arcturus (Hinkle et al. 2000) was convolved by a Gaussian with a dispersion of 1.35 Å. There was no pseudocontinuum associated with the convolved spectrum, and there was excellent agreement between the overall shape of the convolved telluric template and the telluric template used in this paper.

The spectrum of HD 34863 was also used to derive a telluric template to correct the spectra of the G and K giant stars from 8160 to 8400 Å. In this region, the B star spectrum is featureless, and deriving the template was straightforward. This template was applied to the stars using the same method as for the galaxies.

REFERENCES

Alef, W., Goetz, M. M. A., Preuss, E., & Kellermann, K. I. 1988, A&A, 192, 53
Barth, A. J., Ho, L. C., Filippenko, A. V., Rix, H., & Sargent, W. L. W. 2001, ApJ, 546, 205
Barth, A. J., Ho, L. C., & Sargent, W. L. W. 2002, AJ, 124, 2607
Beloborodov, A. M. 1999, ApJ, 510, L123
Bender, R. 1990, A&A, 229, 441
Biermann, P., Preuss, E., Kronberg, P., Schilizzi, R., & Shaffer, D. 1981, ApJ, 250, L49
Boller, T., Meurs, E. J. A., Brinkmann, W., Fink, H., Zimmermann, U., & Adorf, H.-M. 1992, A&A, 261, 57
Bower, G. A., Wilson, A. S., Heckman, T. M., Magorrian, J., Gebhardt, K., Richstone, D. O., Peterson, B. M., & Green, R. F. 2000, BAAS, 32, 1566
Bower, G. A., Wilson, A. S., Heckman, T. M., & Richstone, D. O. 1996, AJ, 111, 1901
Chen, K., & Halpern, J. P. 1989, ApJ, 344, 115
Chen, K., Halpern, J. P., & Filippenko, A. V. 1989, ApJ, 339, 742
Devereux, N., Ford, H., Tsvetanov, Z., & Jacoby, G. 2003, AJ, 125, 1226
Dietrich, M., et al. 1998, ApJS, 115, 185
Dressler, A. 1984, ApJ, 286, 97
Dumont, A. M., & Collin-Souffrin, S. 1990, A&A, 229, 302

Elvis, M., et al. 1994, ApJS, 95, 1
Emsellem, E., Greusard, D., Combes, F., Friedli, D., Leon, S., Pécontal, E., & Wozniak, H. 2001, A&A, 368, 52
Eracleous, M., & Halpern, J. P. 1994, ApJS, 90, 1
———. 1998, in AIP Conf. Proc. 431, Accretion Power in Astrophysical Systems: Some Like it Hot!, ed. S. S. Holt & T. R. Kallman (New York: AIP), 261
———. 2003, ApJ, 599, 886
———. 2004, ApJS, 150, 181
Eracleous, M., Halpern, J. P., & Charlton, J. C. 2003, ApJ, 582, 633
Eracleous, M., Livio, M., Halpern, J. P., & Storchi-Bergmann, T. 1995, ApJ, 438, 610
Ferrarese, L., & Merritt, D. 2000, ApJ, 539, L9
Frank, J., King, A., & Raine, D. J. 2002, Accretion Power in Astrophysics (Cambridge: Cambridge Univ. Press)
Garcia-Rissmann, A., Vega, L. R., Asari, N. V., Fernandes, R. C., Schmitt, H., González Delgado, R. M., & Storchi-Bergmann, T. 2005, MNRAS, 359, 765
Gebhardt, K., et al. 2000, ApJ, 539, L13
Gezari, S. 2005, Ph.D. thesis, Columbia Univ.
Gezari, S., Halpern, J. P., Eracleous, M., & Filippenko, A. V. 2004, in IAU Symp. 222, The Interplay of Black Holes, Stars, and ISM in Galactic Nuclei, ed. T. Storchi-Bergmann, L. C. Ho, & H. R. Schmitt (Cambridge: Cambridge Univ. Press), 95
Gilbert, A. M., Eracleous, M., Filippenko, A. V., & Halpern, J. P. 1999, in ASP Conf. Ser. 175, Structure and Kinematics of Quasar Broad Line Regions, ed. C. M. Gaskell et al. (San Francisco: ASP), 189
Halpern, J. P. 1990, ApJ, 365, L51
———. 1997, in ASP Conf. Ser. 128, Mass Ejection from Active Galactic Nuclei, ed. N. Arav, I. Shlosman, & R. J. Weymann (San Francisco: ASP), 41
Heckman, T. M. 1980, A&A, 87, 152
Hinkle, K., Wallace, L., Valenti, J., & Harmer, D., eds. 2000, Visible and Near Infrared Atlas of the Arcturus Spectrum 3727–9300 Å (San Francisco: ASP)
Ho, L. C. 1999, ApJ, 516, 672
Ho, L. C., Filippenko, A. V., Sargent, W. L. W., & Peng, C. Y. 1997, ApJS, 112, 391
Ho, L. C., Rudnick, G., Rix, H., Shields, J. C., McIntosh, D. H., Filippenko, A. V., Sargent, W. L. W., & Eracleous, M. 2000, ApJ, 541, 120
Horne, K., & Marsh, T. R. 1986, MNRAS, 218, 761
Hummel, E., van der Hulst, J. M., & Keel, W. C. 1987, A&A, 172, 32
Iyomoto, N., Makishima, K., Matsushita, K., Fukazawa, Y., Tashiro, M., & Ohashi, T. 1998, ApJ, 503, 168
Kaspi, S., Smith, P. S., Netzer, H., Maoz, D., Jannuzi, B. T., & Giveon, U. 2000, ApJ, 533, 631
Kassebaum, T. M., Peterson, B. M., Wanders, I., Pogge, R. W., Bertram, R., & Wagner, R. M. 1997, ApJ, 475, 106
Lewis, K. T. 2005, Ph.D. thesis, Pennsylvania State Univ.
Lewis, K. T., Eracleous, M., Halpern, J., & Storchi-Bergmann, T. 2004a, in ASP Conf. Ser. 311, AGN Physics with the Sloan Digital Sky Survey, ed. G. T. Richards & P. B. Hall (San Francisco: ASP), 193
———. 2004b, in IAU Symp. 222, The Interplay of Black Holes, Stars and ISM in Galactic Nuclei (Cambridge: Cambridge Univ. Press), 107
Malaguti, G., Bassani, L., & Caroli, E. 1994, ApJS, 94, 517
Malzac, J., Beloborodov, A. M., & Poutanen, J. 2001, MNRAS, 326, 417
Markoff, S., Falcke, H., & Fender, R. 2001, A&A, 372, L25
Miley, G., Neugebauer, G., Soifer, B. T., Clegg, P. E., Harris, S., Rowan-Robinson, M., & Young, E. 1984, ApJ, 278, L79
Nelson, C. H., Green, R. F., Bower, G., Gebhardt, K., & Weistrop, D. 2004, ApJ, 615, 652
Nemmen, R. S., Storchi-Bergmann, T., Eracleous, M., Terashima, Y., & Wilson, A. 2004, in IAU Symp. 222, The Interplay of Black Holes, Stars, and ISM in Galactic Nuclei (Cambridge: Cambridge Univ. Press), 53
Nemmen, R. S., Storchi-Bergmann, T., Yuan, F., Eracleous, M., Terashima, Y., & Wilson, A. S. 2006, ApJ, in press
Newman, J. A., Eracleous, M., Filippenko, A. V., & Halpern, J. P. 1997, ApJ, 485, 570
Oke, J. B. 1987, in Superluminal Radio Sources, ed. A. J. Zensus & T. J. Pearson (Cambridge: Cambridge Univ. Press), 267
Perez, E., Mediavilla, E., Penston, M. V., Tadhunter, C., & Moles, M. 1988, MNRAS, 230, 353
Pritchet, C. 1978, ApJ, 221, 507
Rees, M. J., Phinney, E. S., Begelman, M. C., & Blandford, R. D. 1982, Nature, 295, 17
Sambruna, R. M., Eracleous, M., & Mushotzky, R. F. 1999, ApJ, 526, 60
Sarzi, M., Rix, H.-W., Shields, J. C., Rudnick, G., Ho, L. C., McIntosh, D. H., Filippenko, A. V., & Sargent, W. L. W. 2001, ApJ, 550, 65
Sergeev, S. G., Pronik, V. I., Peterson, B. M., Sergeeva, E. A., & Zheng, W. 2002, ApJ, 576, 660
Sergeev, S. G., Pronik, V. I., & Sergeeva, E. A. 2000, A&A, 356, 41
Shakura, N. I., & Sunyaev, R. A. 1973, A&A, 24, 337
Shapovalova, A. I., et al. 2001, A&A, 376, 775
Shields, J. C., Rix, H., McIntosh, D. H., Ho, L. C., Rudnick, G., Filippenko, A. V., Sargent, W. L. W., & Sarzi, M. 2000, ApJ, 534, L27
Spergel, D. N., et al. 2003, ApJS, 148, 175
Stauffer, J., Schild, R., & Keel, W. 1983, ApJ, 270, 465
Stocke, J. T., Liebert, J., Gioia, I. M., Maccacaro, T., Griffiths, R. E., Danziger, I. J., Kunth, D., & Lub, J. 1983, ApJ, 273, 458
Storchi-Bergmann, T., Baldwin, J. A., & Wilson, A. S. 1993, ApJ, 410, L11
Storchi-Bergmann, T., Eracleous, M., Livio, M., Wilson, A. S., Filippenko, A. V., & Halpern, J. P. 1995, ApJ, 443, 617
Storchi-Bergmann, T., Eracleous, M., Ruiz, M. T., Livio, M., Wilson, A. S., & Filippenko, A. V. 1997, ApJ, 489, 87
Storchi-Bergmann, T., Nemmen, R. S., Spinelli, P. F., Eracleous, M., Wilson, A. S., Filippenko, A. V., & Livio, M. 2005, ApJ, 624, L13
Storchi-Bergmann, T., et al. 2003, ApJ, 598, 956
Strateva, I. V., et al. 2003, AJ, 126, 1720
Tremaine, S., et al. 2002, ApJ, 574, 740
Veilleux, S., & Zheng, W. 1991, ApJ, 377, 89
Wanders, I., & Peterson, B. M. 1996, ApJ, 466, 174
Worthey, G. 1994, ApJS, 95, 107
Wu, X., & Liu, F. K. 2004, ApJ, 614, 91
York, D. G., et al. 2000, AJ, 120, 1579
Zheng, W. 1996, AJ, 111, 1498
Zheng, W., Veilleux, S., & Grandi, S. A. 1991, ApJ, 381, 418